electric hysteresis loops (experimental). Note that such a large flexoelectric field has been obtained in spite of our conservative choice of flexoelectric coefficients, supporting the feasibility of the flexoelectric switching mechanism. We stress that the Landau formalism provides an upper limit for the ideal (intrinsic) switching barrier; in practice, there will be defects that act as nucleation sites facilitating the switching at lower coercive fields. In real devices, therefore, the effective coercive field may be considerably lower than calculated here, meaning that the flexoelectric field will be capable of inducing switching at lower loads or larger thicknesses than assumed here.

There are several useful features of mechanical switching: (i) It generates stable domain patterns exhibiting no relaxation for days after switching, (ii) mechanically written domain patterns are electrically erasable, (iii) no damage to the sample surface caused by a high loading force was observed, and (iv) the mechanically written domains are nanoscopic. These features are illustrated in Fig. 3. Mechanically written parallel linear domains, shown in Fig. 3A, have been subsequently transformed into the pattern in Fig. 3B by electrically erasing central domain segments with a tip under a dc –3-V bias. The topographic image of the same area of the $BaTiO_3$ film (Fig. 3C), acquired after this procedure, does not exhibit any traces of surface deformation. Finally, Fig. 3D shows an array of dot domains only 30 nm in size, written by abruptly alternating the tip load between 30 and 1500 nN during scanning.

These results open up a way to write ferroelectric memory bits using mechanical force instead of electrical bias in data-storage devices. By converting mechanical stress into readable information, such devices would operate as a nanoscopic analog of typewriters that could be scaled up using a millipede-like scheme (*24*). The tip-sample contact area is typically less than 10-nm in radius, so switching can be highly localized, allowing fabrication of high-density domain patterns. Because no voltage is applied during mechanical switching, leakage and/or dielectric breakdown problems are minimized [in fact, even insulating tips can be used to mechanically write the domains, as shown in fig. S4 (*18*)]. Because electrodes are not required, the problems caused by their finite screening length (*25*) are also removed.

Conversely, if top electrodes were used, mechanical writing would enable the targeted poling of localized areas under the electrodes—which is impossible using voltage, as the electric field is homogeneous in a parallel-plate capacitor. This suggests the possibility of controlled fabrication of domain walls underneath top electrodes, useful for electronic device applications employing physical properties of domain walls (*26*) that could be read in a nondestructive manner by PFM imaging (*27*) or by measuring the electroresistive effect (*28*).

### References and Notes


1. K. J. Choi *et al.*, *Science* **306**, 1005 (2004).
2. G. Catalan *et al.*, *Phys. Rev. Lett.* **96**, 127602 (2006).
3. G. Zavala, J. H. Fendler, S. Trolier-McKinstry, *J. Appl. Phys.* **81**, 7480 (1997).
4. A. Kholkin *et al.*, *Appl. Phys. Lett.* **82**, 2127 (2003).
5. A. Gruverman, A. Kholkin, A. Kingon, H. Tokumoto, *Appl. Phys. Lett.* **78**, 2751 (2001).
6. D. Lee *et al.*, *Phys. Rev. Lett.* **107**, 057602 (2011).
7. A. Gruverman *et al.*, *Appl. Phys. Lett.* **83**, 728 (2003).
8. S. M. Kogan, *Sov. Phys. Solid State* **5**, 2069 (1964).
9. J. F. Scott, *J. Chem. Phys.* **48**, 874 (1968).
10. G. Catalan, L. J. Sinnamon, J. M. Gregg, *J. Phys. Condens. Matter* **16**, 2253 (2004).
11. G. Catalan *et al.*, *Nat. Mater.* **10**, 963 (2011).
12. M. S. Majdoub, P. Sharma, T. Çağin, *Phys. Rev. B* **78**, 121407 (2008).
13. C. B. Eom *et al.*, *Science* **258**, 1766 (1992).
14. L. J. Belenky, X. Ke, M. Rzchowski, C. B. Eom, *J. Appl. Phys.* **97**, 10J107 (2005).
15. In our studies, the flexoelectric switching has been demonstrated in films with thickness of up to 48 unit cells.
16. D. D. Fong *et al.*, *Phys. Rev. Lett.* **96**, 127601 (2006).
17. Y. Gaillard, A. Hurtado Macías, J. Muñoz-Saldaña, M. Anglada, G. Trápaga, *J. Phys. D Appl. Phys.* **42**, 085502 (2009).
18. Supplementary materials are available on *Science* Online.
19. W. Ma, *Phys. Status Solidi B* **245**, 761 (2008).
20. R. Maranganti, P. Sharma, *Phys. Rev. B* **80**, 054109 (2009).
21. W. Ma, L. E. Cross, *Appl. Phys. Lett.* **88**, 232902 (2006).
22. J. Hong, G. Catalan, J. F. Scott, E. Artacho, *J. Phys. Condens. Matter* **22**, 112201 (2010).
23. A. Yu. Emelyanov, N. A. Pertsev, A. L. Kholkin, *Phys. Rev. B* **66**, 214108 (2002).
24. P. Vettiger *et al.*, *IEEE Trans. NanoTechnol.* **1**, 39 (2002).
25. V. Nagarajan *et al.*, *J. Appl. Phys.* **100**, 051609 (2006).
26. G. Catalan, J. Seidel, R. Ramesh, J. F. Scott, *Rev. Mod. Phys.* **84**, 119 (2012).
27. D. A. Bonnell, S. V. Kalinin, A. Kholkin, A. Gruverman, *MRS Bull.* **34**, 648 (2009).
28. V. Garcia *et al.*, *Nature* **460**, 81 (2009).



**Acknowledgments:** A.G and G.C. conceived the idea, designed the experiment, and wrote the paper; H.L. implemented experimental measurements; C.-W.B. fabricated the samples; C.-B.E. supervised sample preparation and reviewed the paper; and D.E.O., J.A., and G.C. performed finite-element and free-energy calculations. G.C. and A.G. thank the Leverhulme Trust for international network funding (F/00 203/V) for the funds that have enabled this collaboration. G.C. acknowledges financial support from grants MAT2010-10067-E and MAT2010-17771, and J.A. acknowledges support from grant MAT2011-23375 (Ministerio de Educación, Ciencia e Innovación). The work at Univ. of Nebraska-Lincoln was supported by the Materials Research Science and Engineering Center (NSF grant DMR-0820521) and by the U.S. Department of Energy (DOE), Office of Basic Energy Sciences, Division of Materials Sciences and Engineering (DOE grant DE-SC0004876). The work at Univ. of Wisconsin–Madison was supported by the NSF under grant ECCS-0708759.


### Supplementary Materials

www.sciencemag.org/cgi/content/full/336/6077/59/DC1
Materials and Methods
Supplementary Text
Figs. S1 to S4
References

4 January 2012; accepted 23 February 2012
10.1126/science.1218693



# High-Resolution EM of Colloidal Nanocrystal Growth Using Graphene Liquid Cells

Jong Min Yuk,[1,2,3]* Jungwon Park,[2,4]* Peter Ercius,[5] Kwanpyo Kim,[1,2,6] Daniel J. Hellebusch,[4] Michael F. Crommie,[1,2,6] Jeong Yong Lee,[3]† A. Zettl,[1,2,6]† A. Paul Alivisatos[2,4]†

We introduce a new type of liquid cell for in situ transmission electron microscopy (TEM) based on entrapment of a liquid film between layers of graphene. The graphene liquid cell facilitates atomic-level resolution imaging while sustaining the most realistic liquid conditions achievable under electron-beam radiation. We employ this cell to explore the mechanism of colloidal platinum nanocrystal growth. Direct atomic-resolution imaging allows us to visualize critical steps in the process, including site-selective coalescence, structural reshaping after coalescence, and surface faceting.

A wide range of physical, chemical, and biological phenomena that take place in liquids on the nanometer scale would benefit from observations with atomic resolution transmission electron microscopy (TEM). EM techniques such as conventional TEM (CTEM), scanning TEM (STEM), and four-dimensional (4D) EM have enabled direct observation of solid-phase phenomena with atomic resolution (*1*–*4*). Applying these effective imaging tools to the study of liquid-phase phenomena is hampered by difficulties in maintaining realistic conditions for the liquid specimen (*5*). For example, TEM requires high vacuum conditions, which are generally incompatible with liquid samples. One way to overcome this constraint is to employ environmental cells that contain a sealed reservoir with a viewing window fabricated from $Si_3N_4$ or $SiO_2$ (*6*–*8*). Although such liquid cells have enabled studies of nanoscale phenomena, the relatively thick (tens to one hundred nanometers) and relatively high atomic number ($Z$) element windows have poor electron transmittance, resulting in reduced sensitivity and a resolution limit of a few nanometers. Unfortunately, true atomic-resolution imaging cannot be achieved, and furthermore, the thick cell windows also appear to perturb the natural state of the liquid or species suspended in the liquid.

An example of the benefits that could arise from atomic-resolution imaging in nonperturbative

liquid cells presents itself in the growth of colloidal inorganic nanocrystals, such as Pt. The first movies of colloidal nanocrystal growth (*7*), restricted to lower resolution, revealed unexpected phenomena, namely that the colloidal Pt particles grow by frequent particle coalescence events and, most surprisingly, that the particle growth apparently pauses after a coalescence event. The reason for this apparent pause was attributed to possible structural rearrangements within the coalescing nanocrystals, but this conjecture could not be proven.

Recently developed protocols for the high-yield fabrication of subnanometer-thick suspended membranes such as graphene, graphene oxide, and boron nitride (*9*–*11*) have provided the ultimate transparent sample supports for EM (*12*–*15*). Graphene that has a thickness of one carbon atom ($Z = 6$) is the thinnest of these membranes. When used as a support for TEM specimens, graphene provides a high contrast for any type of material including isolated light atoms and organic molecules (*1*, *16*, *17*). Moreover, it is straightforward to employ graphene membranes for encapsulating gas, liquid, or solid materials for ambient- and vacuum-condition experiments due to their high flexibility, mechanical tensile strength, and impermeability to small molecules (*18*, *19*). In addition, graphene is also an excellent electrical and thermal conductor and displays minimal charging and heating effects under the electron beam (*17*). An inherently inert surface eliminates chemical and physical interference from the substrate. Here, we introduce the graphene liquid cell (GLC) as a real-time reaction chamber to study atom-resolved colloidal nanocrystal growth and dynamics with an aberration-corrected transmission electron microscope.

The high-resolution liquid cell is prepared by encapsulating a Pt growth solution between two laminated graphene layers suspended over holes in a conventional TEM grid. An example of the GLC is illustrated in Fig. 1: The TEM micrograph shows the encapsulated liquid sample (area with darker contrast) trapped between two suspended graphene sheets (lighter contrast) (Fig. 1A), accompanied by an idealized illustration (Fig. 1B). Graphene is grown on a copper foil substrate via chemical vapor deposition (*20*) and then directly transferred onto a gold TEM mesh with a perforated amorphous carbon support (*21*). The stock Pt growth solution (*7*) is pipetted directly atop two graphene-coated TEM grids facing in opposite directions (fig. S1A). Upon wetting the system, the solution wicks between the graphene and amorphous carbon layers, allowing one of the graphene membranes to detach from its associated TEM grid (*22*). Because the van der Waals interaction between graphene sheets is relatively strong (*23*), liquid droplets of various thickness from 6 to 200 nm can be securely trapped between a double-membrane liquid pocket or blister (Fig. 1 and figs. S1B and S2). Although our GLCs are typically composed of monolayer graphene at the top and bottom interfaces, large surface strain imposed on the detached graphene by the solution can also cause the edge of the graphene sheet to curl up on itself many times, creating a nanoscroll, which in turn creates, if desired, multimembrane protected liquid pockets (fig. S1B, inset) (*24*). Generally, for our GLCs, the graphene remains fully intact throughout the fabrication process, as indicated by a relatively low defect-induced graphene D peak (around 1350 $cm^{-1}$) observed in Raman spectra (fig. S3).

We image Pt nanocrystal growth and dynamics in as-prepared GLCs on the Transmission Electron Aberration-Corrected Microscope I (TEAM I) managed by the National Center for Electron Microscopy. The microscope is operated at 80 kV with a beam intensity of $10^3$ to $10^4$ $A/m^2$ maintained during nanocrystal growth. Upon locating a liquid pocket on the TEM grid, the beam intensity is optimized, which reduces the Pt precursor and initiates nanocrystal growth (*7*). The graphene membrane with encapsulated liquid remains intact over the entire time period of TEM observation, ensuring prolonged (at least tens of minutes) high-resolution in situ imaging. Spherical and chromatic aberration correctors on TEAM I further contribute to the exceptionally high resolution and enhanced signal-to-noise ratio (*25*).

Extended movies of colloidal Pt nanocrystal growth (movies S1 and S2) reveal major differences between data collected with the use of GLCs compared with previous cells with silicon nitride windows (*7*), even at the earliest stages of the colloidal Pt nanocrystal growth. It is possible

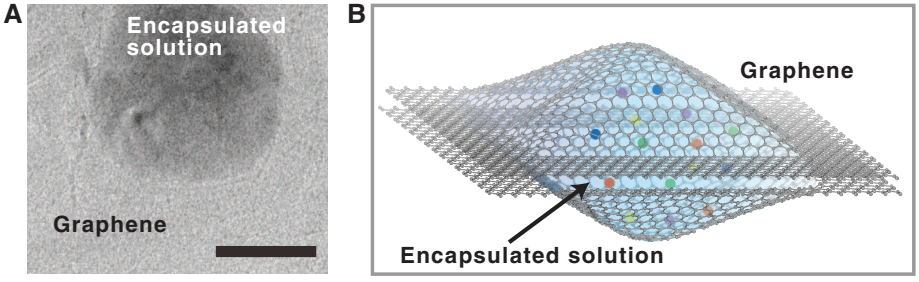


**Fig. 1.** (**A**) TEM image of a GLC; laminated graphene layers immobilize a blister of encapsulated stock solution (dark region). Scale bar, 50 nm. (**B**) Idealized illustration of local GLCs encapsulating growth solution.

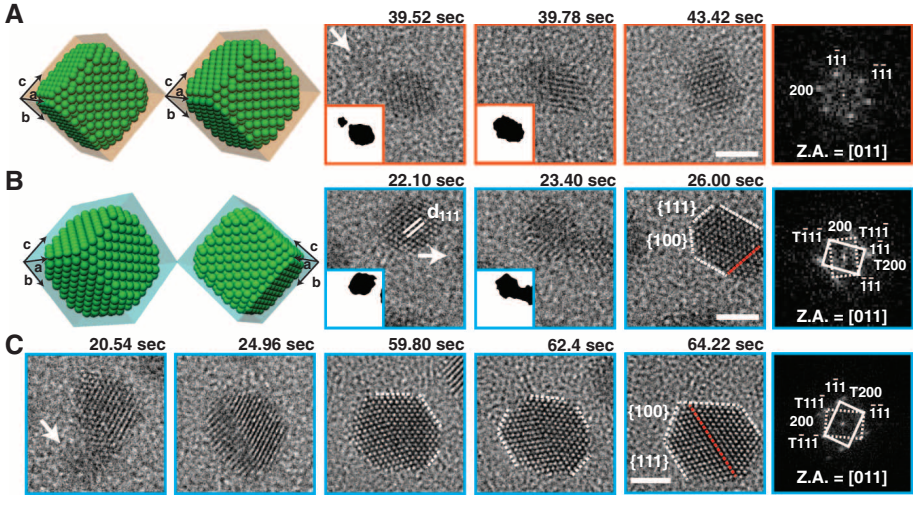


**Fig. 2.** Still snapshots from movie S2 of Pt nanocrystal growth via coalescence and crystal-structure evolution observed with atomic resolution in a GLC. Schematic illustrations and corresponding TEM images exhibiting nanocrystal coalescence along the <111> direction, evolving into (**A**) a single crystalline fcc structure or (**B**) a twinned (red dotted line) fcc structure. (**C**) Shape evolution of the Pt nanocrystal by straightening of the twin boundary (red dotted line) and evolution toward a hexagonal shape. The rightmost panel in each sequence shows a FFT of the panel adjacent to it. White arrows denote incoming small nanocrystals (as seen in insets). Scale bars, 2 nm. Z.A., zone axis.

[1]Department of Physics, University of California at Berkeley, Berkeley, CA 94720, USA. [2]Materials Sciences Division, Lawrence Berkeley National Laboratory, Berkeley, CA 94720, USA. [3]Department of Materials Science and Engineering, KAIST, Daejeon, 305-701, South Korea. [4]Department of Chemistry, University of California at Berkeley, Berkeley, CA 94720, USA. [5]National Center for Electron Microscopy, Lawrence Berkeley National Laboratory, Berkeley, CA 94720, USA. [6]Center of Integrated Nanomechanical Systems, University of California at Berkeley, Berkeley, CA 94720, USA.

*These authors contributed equally to this work.
†To whom correspondence should be addressed. E-mail: j.y.lee@kaist.ac.kr (J.Y.L.); azettl@berkeley.edu (A.Z.); alivis@berkeley.edu (A.P.A.)

to discern colloidal Pt nanoparticles with radii as small as 0.1 nm and to track their motion. Using silicon nitride window cells, the nanoparticle motion is perturbed by the windows; nanoparticles of Au and Pt in such cells have been observed to remain localized close to one of the windows, weakly bound to the surface layer, and to execute complex non-Brownian motion near the window (*7*, *26*). In contrast, the interaction of the nanoparticles with graphene is weaker, and the motion of the colloidal Pt nanoparticles while growing by monomer attachment is not influenced by association with the window (see supplementary materials).

The nanocrystals grow by both monomer addition and frequent coalescence events (figs. S4 to S6). Using the GLC, it is possible to directly observe critically important features of the coalescence process that could not be resolved in earlier studies. We first examine the crystallographic orientation relationship of nanocrystals during their coalescence. Figure 2 shows TEM images of in situ Pt nanocrystal growth by coalescence. Incoming small nanocrystals are marked with white arrows on TEM images and can be seen clearly in black/white color mapped insets for the nanocrystal and background. Once nanocrystals collide at {111} planes, they merge quickly, within 0.26 s (the limit of our acquisition time). We observe that most coalescence events proceed along the same crystallographic direction, indicating that there is a specific nanocrystal orientation for coalescence (movie S2). This result is notable, because {111} planes of a face-centered cubic (fcc) crystal have the lowest surface energy. This behavior may be due to different degrees of ligand coverage on different nanocrystal factes; {111} planes of a fcc crystal have the lowest surface energy and, therefore, perhaps the lowest ligand coverage. In this scenario, nanocrystals that contact at {111} planes experience minimal ligand obstruction and hence quickly unify to minimize the total surface area—and, thus, overall surface energy (*27*). Coalescence in this manner proceeds in one of two ways: The first is contact that joins identical, or mirror, {111} planes. Nanocrystals captured in Fig. 2A exemplify this, which results in a perfectly aligned crystal with a single crystallographic domain, as shown in the fast Fourier transformed (FFT) pattern. The second case, as seen in Fig. 2, B and C, yields nanocrystals with a twin boundary; the corresponding FFTs reveal two double domains. For the duration of our movies, twin boundaries formed from coalescence remain locked within the nanocrystal. The interface energy of the twin boundary is known to be thermodynamically non-negligible (*27*). However, it appears that, under the present experimental conditions, structural rearrangements of the nanoparticles occur mainly by surface rearrangements and not by reorganization of the complete nanocrystal interior. Misoriented particle coalescence appears to account for the formation mechanism of twin boundaries commonly observed in synthesized fcc metal nanocrystals (*27*).

Before coalescing along the {111} orientation, the nanocrystals exhibit a prolonged period of correlated motion that facilitates lattice alignment and unification. We track size and position change (Fig. 3) of two nanocrystals before they coalesce at the subnanometer range. In Fig. 3A, two nanocrystals show correlated rather than independent motion over a 100-s interval, culminating in lattice alignment and coalescence. The correlated motion presumably arises because of interparticle attractive forces. Based on theoretical studies, the attractive forces can be attributed to van der Waals interactions, steric repulsions, and depletion forces arising from surface ligands (*28*). The duration of the correlated motions that we observe in movies S1 and S2 varies depending on nanocrystal size and the local thickness of the liquid medium. We measure the center-to-center distance (red circles in Fig. 3A) between two adjacent nanocrystals from a position plot of the two nanocrystals (Fig. 3B). Comparison of this distance with nanocrystal size provides insight into the mechanisms of nanocrystal growth by coalescence. As the freely moving nanocrystals seen in movie S1 draw close, the center-to-center distance rapidly decreases. This initial event occurs within 40 s, and the center-to-center separation fluctuates between 4 to 6 nm for the next 25 s. While this dynamic event proceeds, the nanocrystals also grow in size from ~0.75 to 1 nm in diameter due to monomer addition. The surface ligand, oleylamine, is known to be 1 to 2 nm long, depending on the orientation and extension of its floppy alkyl chain and surface-packing density (*29*). Therefore, the sustained correlated motion occurs with weakly touching surface ligand layers (*30*). The center-to-center distance shows even more confined fluctuation of ~1 nm in the time interval from 80 to 130 s. In this time range, we observe that the correlated motion of the two nanocrystals exhibits 3D behavior of rolling and relative sliding of nanocrystals over each other. Throughout this period, the nanocrystals continue to grow by monomer addition, continuously increasing the attractive force between the particles. After 130 s, the center-to-center distance approaches the sum of the radii of the two nanocrystals, and the nanocrystal lattices align, leading to coalescence at 160 s.

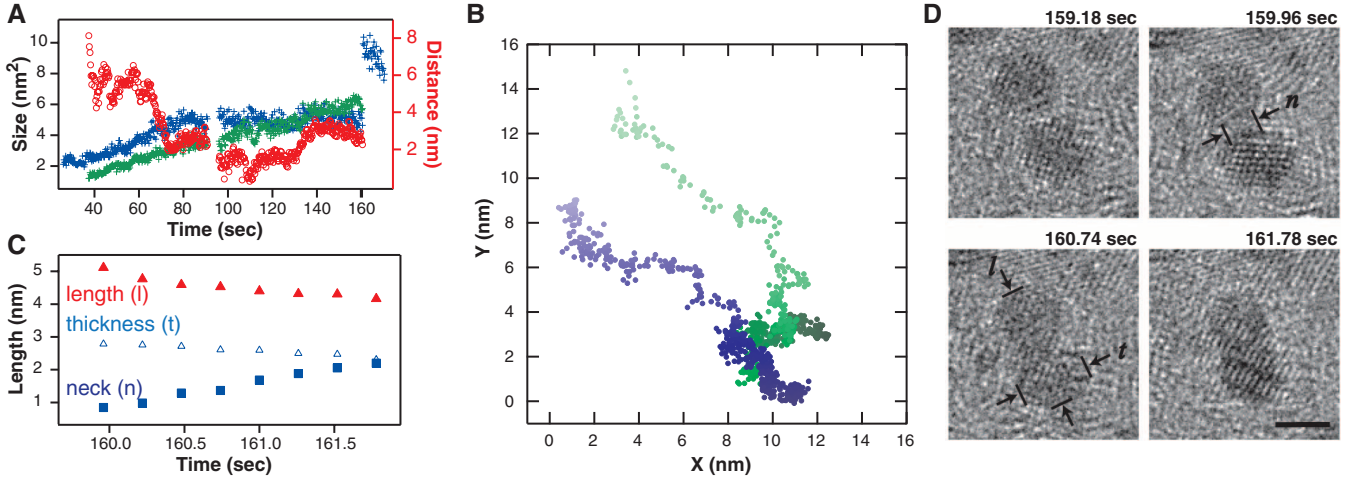


**Fig. 3.** Pt nanocrystal dynamics before (**A** and **B**) and after (**C** and **D**) coalescence. (A) Projected distance between two nanocrystals (red) up until the two nanocrystals coalesce, as well as the size [blue and green, area (square nanometers) is measured for spherical and ellipsoidal nanocrystal shapes before and after coalescence, respectively] of the two nanocrystals during the period of correlated motion. The nanocrystal labeled in green merges with the blue-labeled nanocrystal at 160 s. Two consecutive movie clips were merged into movie S1, accounting for the data gap of 5 s at the 95-s point. (B) Two-dimensional projected position change of the two nanocrystals before coalescence. Blue and green correspond to the nanocrystals in (A), with the color gradient for time evolution from 40 s (bright) to 160 s (dark). Still snapshots for different stages can be found in fig. S7. (C) Neck diameter (*n*), thickness (*t*), and length (*l*) after the coalescence of the two nanocrystals. The time domain of this plot corresponds to the interval over which the apparent nanocrystal size decreases after coalescence in (A). (D) Still snapshots from movie S1 corresponding to (C). Scale bar, 2 nm.

Single-particle growth trajectories in the one previous lower-resolution study of Pt nanocrystal growth showed an apparent size decrease after coalescence, as well as a short pause after coalescence before apparent growth by monomer attachment has resumed (fig. S4) (*7*). In the GLC, it is possible to examine and understand in much more detail these unexpected phenomena that follow nanoparticle coalescence. Figure 3C is a plot of the change in length (*l*, along the center-to-center direction), thickness (*t*, vertical direction to the length), and neck diameter (*n*) of the coalesced nanocrystals, whereas Fig. 3D shows the corresponding TEM images. The nanocrystals are connected by a neck at the initial stage of coalescence. Neck growth is accompanied by a decrease in *l* and *t*, which indicates that the atoms migrate to the neck region, presumably by surface diffusion (*31*). After coalescence, the nanocrystal structure also gradually reorganizes, evolving truncated surfaces. Returning to Fig. 2C, the nanocrystal shape after coalescence changes from quasi-spherical to a hexagonal shape that minimizes the surface energy of the nanocrystal as expected from a Wulff construction, also by surface-diffusion processes.

We introduce the GLC as a new type of liquid cell advancing the imaging of liquid-phase systems; encapsulated liquid specimens are observed with an electron microscope at the highest resolution possible to date with minimal sample perturbation. The GLC has enabled the study of colloidal nanocrystal growth with unprecedented resolution, revealing a host of previously unexpected phenomena. We have directly observed the steps of nanocrystal coalescence and oriented attachment at an atomic level. The GLC can be readily applied to directly study a diversity of fluid-phase samples, which beg detailed observation.

### References and Notes


1. J. C. Meyer, C. O. Girit, M. F. Crommie, A. Zettl, *Nature* **454**, 319 (2008).
2. C.-Y. Wen *et al.*, *Science* **326**, 1247 (2009).
3. V. Radmilovic *et al.*, *Nat. Mater.* **10**, 710 (2011).
4. A. H. Zewail, *Science* **328**, 187 (2010).
5. N. de Jonge, F. M. Ross, *Nat. Nanotechnol.* **6**, 695 (2011).
6. M. J. Williamson, R. M. Tromp, P. M. Vereecken, R. Hull, F. M. Ross, *Nat. Mater.* **2**, 532 (2003).
7. H. Zheng *et al.*, *Science* **324**, 1309 (2009).
8. J. E. Evans, K. L. Jungjohann, N. D. Browning, I. Arslan, *Nano Lett.* **11**, 2809 (2011).
9. K. S. Novoselov *et al.*, *Proc. Natl. Acad. Sci. U.S.A.* **102**, 10451 (2005).
10. X. Li *et al.*, *Nat. Nanotechnol.* **3**, 538 (2008).
11. J. N. Coleman *et al.*, *Science* **331**, 568 (2011).
12. Z. Lee *et al.*, *Nano Lett.* **9**, 3365 (2009).
13. A. Kolmakov *et al.*, *Nat. Nanotechnol.* **6**, 651 (2011).
14. Y. A. Wu *et al.*, *Nanotechnology* **22**, 195603 (2011).
15. J. C. Meyer, C. O. Girit, M. F. Crommie, A. Zettl, *Appl. Phys. Lett.* **92**, 123110 (2008).
16. R. Erni *et al.*, *Phys. Rev. B* **82**, 165443 (2010).
17. R. R. Nair *et al.*, *Appl. Phys. Lett.* **97**, 153102 (2010).
18. J. M. Yuk *et al.*, *Nano Lett.* **11**, 3290 (2011).
19. K. Xu, P. Cao, J. R. Heath, *Science* **329**, 1188 (2010).
20. X. Li *et al.*, *Science* **324**, 1312 (2009).
21. W. Regan *et al.*, *Appl. Phys. Lett.* **96**, 113102 (2010).
22. X. Xie *et al.*, *Nano Lett.* **9**, 2565 (2009).
23. S. P. Koenig, N. G. Boddeti, M. L. Dunn, J. S. Bunch, *Nat. Nanotechnol.* **6**, 543 (2011).
24. J. C. Meyer *et al.*, *Nature* **446**, 60 (2007).
25. E. A. Stach, *Mater. Today* **11**, 50 (2008).
26. H. Zheng, S. A. Claridge, A. M. Minor, A. P. Alivisatos, U. Dahmen, *Nano Lett.* **9**, 2460 (2009).
27. X. Lu, M. Rycenga, S. E. Skrabalak, B. Wiley, Y. Xia, *Annu. Rev. Phys. Chem.* **60**, 167 (2009).
28. K. J. M. Bishop, C. E. Wilmer, S. Soh, B. A. Grzybowski, *Small* **5**, 1600 (2009).
29. X. Lu, M. S. Yavuz, H.-Y. Tuan, B. A. Korgel, Y. Xia, *J. Am. Chem. Soc.* **130**, 8900 (2008).
30. P. Schapotschnikow, R. Pool, T. J. H. Vlugt, *Nano Lett.* **8**, 2930 (2008).
31. Z. Z. Fang, H. Wang, *Int. Mater. Rev.* **53**, 326 (2008).


**Acknowledgments:** Work on preparation of a nanocrystal growth solution, portions of the design and construction of GLCs, and data analysis was supported by the Physical Chemistry of Inorganic Nanoscrystals Program, KC3105, Director, Office of Science, Office of Basic Energy Sciences, of the U.S. Department of Energy (DOE) under contract DE-AC02-05CH11231. Portions of the present study were performed at the National Center for Electron Microscopy, Lawrence Berkeley National Laboratory, which is supported by the DOE under contract no. DE-AC02-05CH11231. J.M.Y. and J.Y.L. acknowledge the financial support from Priority Research Centers Program through the National Research Foundation of Korea funded by the Ministry of Education, Science and Technology (grant no. 2010-0029714). A.Z. acknowledges support from the Director, Office of Energy Research, Office of Basic Energy Sciences, Materials Sciences and Engineering Division, of the DOE under contract DE-AC02-05CH11231, which provided for the design and construction of the GLC, and support from the Office of Naval Research under grant N00014-09-1-1066, which provided for graphene growth and spectral characterization. K.K. received further support from the NSF (grant EEC-0832819) for preliminary TEM imaging and analysis.

### Supplementary Materials

www.sciencemag.org/cgi/content/full/336/6077/61/DC1
Materials and Methods
Supplementary Text
Figs. S1 to S12
References (*32*)
Movies S1 and S2

8 December 2011; accepted 27 February 2012
10.1126/science.1217654



# Copper Systematics in Arc Magmas and Implications for Crust-Mantle Differentiation

**Cin-Ty A. Lee,[1]* Peter Luffi,[1] Emily J. Chin,[1] Romain Bouchet,[1,2] Rajdeep Dasgupta,[1] Douglas M. Morton,[3] Veronique Le Roux,[1,4] Qing-zhu Yin,[5] Daphne Jin[1,6]**

**Arc magmas are important building blocks of the continental crust. Because many arc lavas are oxidized, continent formation is thought to be associated with oxidizing conditions. On the basis of copper's (Cu's) affinity for reduced sulfur phases, we tracked the redox state of arc magmas from mantle source to emplacement in the crust. Primary arc and mid-ocean ridge basalts have identical Cu contents, indicating that the redox states of primitive arc magmas are indistinguishable from that of mid-ocean ridge basalts. During magmatic differentiation, the Cu content of most arc magmas decreases markedly because of sulfide segregation. Because a similar depletion in Cu characterizes global continental crust, the formation of sulfide-bearing cumulates under reducing conditions may be a critical step in continent formation.**

The composition and oxidation state of melts formed in subduction zones, collectively known as arc magmas, influence the formation and evolution of the continents, ore deposits, and possibly even the atmosphere (*1*). Arc magmas are oxidized relative to the average upper mantle; however, the means by which these lavas become oxidized is debated. The prevailing view is that arc magmas inherit their oxidized states from melting sub-arc mantle contaminated by subducted sediments and oceanic crust (*1*–*5*). Alternatively, primary arc magmas may be less oxidized than their more evolved counterparts if oxidation is caused by magmatic differentiation associated with crystallization and chemical interaction with preexisting crust (*6*–*9*).

To resolve this debate, the redox state of the mantle source regions of arc magmas must be determined. Unfortunately, primary arc magmas recording this signature are rare because by the time they have risen to the surface, they have already differentiated. One approach has been to investigate the redox state of melts trapped in phenocrysts (*4*), but melt inclusions rarely represent true primary magmas and are found only in extrusive rocks, which may not be representa-

[1]Department of Earth Science, Rice University, MS-126, 6100 Main Street, Houston, TX 77005, USA. [2]Laboratoire de Géologie de Lyon, Ecole Normale Supérieure de Lyon and Université Claude Bernard Lyon 1, CNRS UMR 5276, 46 Allée d'Italie, 69007 Lyon, France. [3]Department of Earth Sciences, University of California Riverside, 900 University Avenue, Riverside, CA 92521, USA. [4]Woods Hole Oceanographic Institution, 266 Woods Hole Road, Woods Hole, MA 02543, USA. [5]Department of Geology, University of California, Davis, CA 95616, USA. [6]William P. Clements High School, Sugar Land, TX 77479, USA.

*To whom correspondence should be addressed. E-mail: ctlee@rice.edu